Seeing the Hidden Lamina: Effects of Exsanguination on the Optic Nerve Head

Huong Tran,[1,2] Jacob Wallace,[2] Ziyi Zhu,[2] Katie A. Lucy,[3] Andrew P. Voorhees,[2] Samantha E. Schmitt,[2] Richard A. Bilonick,[2] Joel S. Schuman,[3] Matthew A. Smith,[1,2] Gadi Wollstein,[3] and Ian A. Sigal[1,2]

[1]Department of Bioengineering, University of Pittsburgh, Pittsburgh, Pennsylvania, United States
[2]Department of Ophthalmology, University of Pittsburgh, Pittsburgh, Pennsylvania, United States
[3]New York University Langone Eye Center, NYU School of Medicine, New York, New York, United States

Correspondence: Ian A. Sigal, Laboratory of Ocular Biomechanics, Department of Ophthalmology, University of Pittsburgh Medical Center, Eye & Ear Institute, 203 Lothrop Street, Room 930, Pittsburgh, PA 15213, USA; ian.sigal@gmail.com.

Submitted: November 10, 2017
Accepted: March 19, 2018

Citation: Tran H, Wallace J, Zhu Z, et al. Seeing the hidden lamina: effects of exsanguination on the optic nerve head. *Invest Ophthalmol Vis Sci*. 2018;59:2564–2575. https://doi.org/10.1167/iovs.17-23356

Purpose. To introduce an experimental approach for direct comparison of the primate optic nerve head (ONH) before and after death by exsanguination.

Method. The ONHs of four eyes from three monkeys were imaged with spectral-domain optical coherence tomography (OCT) before and after exsanguination under controlled IOP. ONH structures, including the Bruch membrane (BM), BM opening, inner limiting membrane (ILM), and anterior lamina cribrosa (ALC) were delineated on 18 virtual radial sections per OCT scan. Thirteen parameters were analyzed: scleral canal at BM opening (area, planarity, and aspect ratio), ILM depth, BM depth; ALC (depth, shape index, and curvedness), and ALC visibility (globally, superior, inferior, nasal, and temporal quadrants).

Results. All four ALC quadrants had a statistically significant improvement in visibility after exsanguination (overall $P < 0.001$). ALC visibility increased by 35% globally and by 36%, 37%, 14%, and 4% in the superior, inferior, nasal, and temporal quadrants, respectively. ALC increased 4.1%, 1.9%, and 0.1% in curvedness, shape index, and depth, respectively. Scleral canals increased 7.2%, 25.2%, and 1.1% in area, planarity, and aspect ratio, respectively. ILM and BM depths averaged −7.5% and −55.2% decreases in depth, respectively. Most, but not all, changes were beyond the repeatability range.

Conclusions. Exsanguination allows for improved lamina characterization, especially in regions typically blocked by shadowing in OCT. The results also demonstrate changes in ONH morphology due to the loss of blood pressure. Future research will be needed to determine whether there are differences in ONH biomechanics before and after exsanguination and what those differences would imply.

Keywords: exsanguination, optic nerve head, lamina cribrosa, OCT, blood vessel shadow

The optic nerve head (ONH) and the lamina cribrosa (LC) within are central to the physiology and pathophysiology of the eye and have, therefore, been the focus of numerous studies.[1–6] Due to technical limitations and ethical considerations, the majority of these studies have been experiments on ocular tissues after death.[5,7–10] Almost invariably, this means enucleating the globe to study the whole[7–9,11] or to be cut and sectioned into small parts.[10,12–14] Recent advances in imaging technologies, especially of optical coherence tomography (OCT), have dramatically increased the power to study the eyes in vivo.[1,15,16] Hence, current knowledge of the ONH and LC is a mix of lessons learned from in vivo and ex vivo experiments, supplemented by analytic and computational modeling.[17,18] It seems reasonable to expect that there may be important and substantial differences between the in vivo and ex vivo conditions. For example, ocular tissues can degrade, swell or dehydrate over time, shrink during preservation, or distort during histologic processing. From a biomechanic perspective, enucleated globes are no longer subjected to the forces from intraocular, cerebrospinal, arterial, venous, episcleral, and orbital pressures, or from the muscles or eyelid action. Although it may be possible to mimic some of these forces in experiments, these are unlikely to reproduce all the complexity of the in vivo environment. To the best of our knowledge, the differences in the ONH and LC between in vivo and ex vivo conditions remain largely unknown. This precludes proper interpretation of the findings in one condition and an understanding of their implications on the other. It is fundamental to understand how measurements in vivo and ex vivo relate to one another.

Herein, we introduce an experimental approach that allows direct comparison of the primate ONH before and after death. Specifically, we imaged with OCT the posterior pole of healthy monkeys before and after death by exsanguination. We then analyzed the images to determine whether there were differences in ONH morphology between the before and after exsanguination scans.

The use of exsanguination to cause death allowed us to leverage the OCT scans for a secondary goal: to test the hypothesis that exsanguination will result in improved visibility of the LC in the OCT scans. It is well known that a major challenge for visualizing the deep ONH structures with OCT is the presence of "shadows" caused by blood. Various post-processing methods have been proposed to enhance LC

Table 1. Pressure Measurements

Eye	IOP, mm Hg	ICP, mm Hg
M1 OD		
Alive	15	10
After life	15	−2
M2 OS		
Alive	15	12
After life	15	2
M3 OD		
Alive	–	13
After life	–	–
M3 OS		
Alive	–	13
After life	–	–

Dash symbol (–) means there was no cannulation of IOP or recording of ICP, as explained in the main text. OD, oculus dexter; OS, oculus sinster.

visibility[19,20] or to estimate LC parameters that cannot be measured in vivo from those that can.[21] Nevertheless, an experimental approach quantifying the changes in LC visualization resulting from removal of the blood, without the need for postprocessing, has not been reported. Improving LC visualization in this manner has the potential to be a valuable research tool, informing the understanding of the intact LCs, because it tells us about what has been difficult or impossible to visualize in vivo and how it relates to what can be visualized.

Methods

Overall Strategy

The ONHs of four eyes of three healthy adult rhesus macaque monkeys were imaged with OCT before (alive), during, and after exsanguination (after life). ONH structures were manually delineated on the OCT scans, and the morphology and visibility of the tissues were characterized by 13 parameters of interest (Fig. 1). We then analyzed the parameters to determine if there were differences between the alive and after life parameters.

Animal Handling and Pressure Set Up

All procedures were approved by the University of Pittsburgh's Institutional Animal Care and Use Committee and adhered to both the guidelines established in the National Institute of Health's Guide for the Care and Use of Laboratory Animals and the Association for Research in Vision and Ophthalmology statement on the use of animals in ophthalmic and vision research. Before the experiment, a clinical examination was conducted to ensure the normal clinical appearance of each monkey's eyes.

The animal was initially sedated with ketamine (20 mg/kg), diazepam (1 mg/kg), and atropine (0.04 mg/kg). The animal was then maintained on isoflurane (1%–3%) for the remainder of the experiment. An arterial line was then placed in the animal's carotid or femoral artery. This allowed for continuous recording of the intra-arterial pressure. After the arterial line was placed, the animal was put on a ventilator and was given a paralytic intravenously (vecuronium bromide, 2 mL/hour) to reduce eye movement. To record and control intracranial pressure (ICP), two small craniotomies were performed to insert a catheter (EDM Lumbar Catheter; Medtronic, Minneapolis, MN) into the lateral ventricle and a sensor (Precision Pressure Catheter; Raumedic, Mills River, NC, USA) nearby into the parenchyma of the brain. The catheter, after establishing flow, was connected to a saline reservoir for ease of manipulating ICP. For the alive-condition imaging, ICP was set to 10 to 13 mm Hg and monitored throughout the exsanguination. In two of the three animals, IOP was controlled by inserting a 27-gauge needle into the anterior chamber and connected to another saline reservoir (Table 1). Between the needle and the saline reservoir, a transducer was placed to record IOP. IOP was then set to 15 mm Hg throughout the experiment. In the third animal (M3), there was no cannulation of the globe and IOP was left at physiologic level. IOP, ICP, and blood pressure were measured and continuously recorded digitally at a rate of 100 Hz (MPR 1 DATALOGGER; Raumedic).

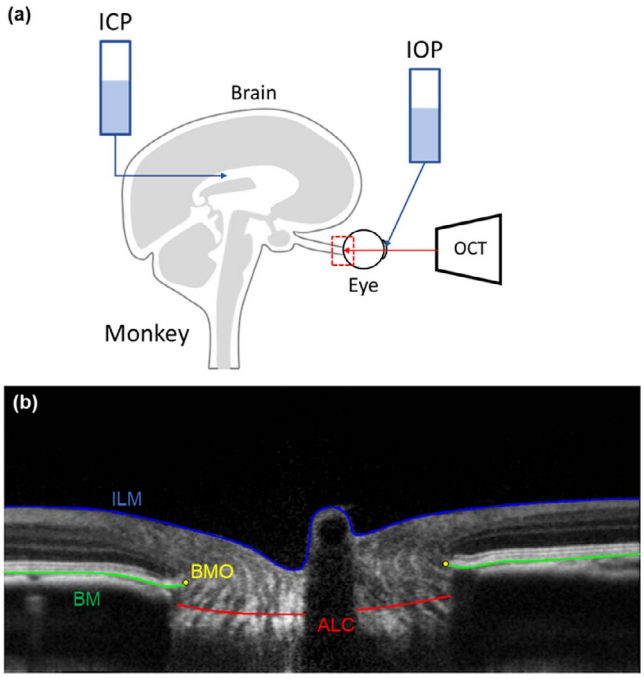

Figure 1. (**a**) Experimental set up. (**b**) An example OCT virtual radial slice with example markings of the ILM (*blue*), BM (*green*), BMO (*yellow*), and the ALC (*red*).

Exsanguination

Prior to the start of the exsanguination, 3000 to 5000 units of heparin were given intravenously. The intravenous saline drip was also left open during the exsanguination to assist flow. Suction was then added to the arterial line with a vacuum pressure of 584 mm Hg. The valve was periodically closed to get a blood pressure reading and the suction was then continued. Animal death was defined as the moment when there was no longer a heartbeat or a blood pressure reading and no pulsation of blood vessels on the OCT viewer. The arterial lines used for exsanguination were placed on two locations, which was found to affect exsanguination time. Specifically, the exsanguination times were 15 and 25 minutes in monkey 1 (M1) and monkey 2 (M2), respectively, in which the arterial line was placed in the carotid artery, and 60 minutes in monkey 3 (M3), in which it was placed in the femoral artery.

Imaging and Image Processing

A rigid gas-permeable contact lens was inserted in each eye (Boston EO, Boston, MA, USA), and the eyes were irrigated

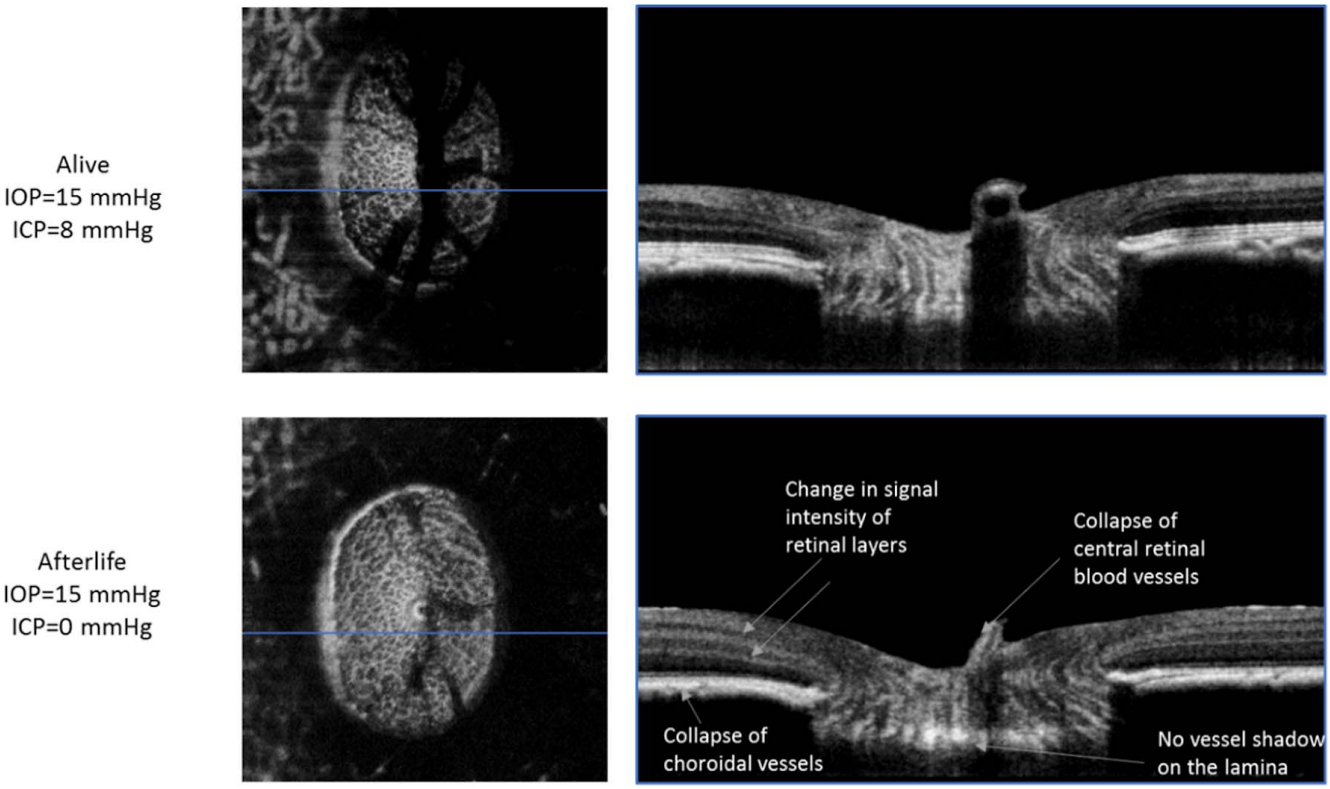

Figure 2. Example C-modes and B-scans comparing ONH structures between alive (*top row*) and after life (*bottom row*) conditions.

with saline every 5 minutes. Images were acquired with spectral-domain OCT (Bioptigen, Research Triangle, NC, USA) modified with a broadband superluminescent diode light source (Superlum, Dublin, Ireland; $\lambda = 870$ nm, $\Delta\lambda = 200$ nm). Raster scans of 3 mm × 3 mm × 1.6 mm (512 × 512 × 1024 pixels sampling) focused on the ONH region were acquired every 1 to 2 minutes. Specifically, the lateral resolution was 5.86 μm/pixel and the axial resolution was 1.56 μm/pixel. Multiple scans were obtained at each timepoint and the best quality scan was selected for delineation.

All OCT scans were scaled to render isotropic pixels. Motion artifacts, resulting from breathing and heart rate, were manually detected by marking the peripheral Bruch membrane (BM) in the orthogonal direction (superior–inferior cross section). This BM delineation was then used to guide the automatic translation of B-scans in the anterior–posterior direction by using custom Matlab (Mathworks, Natick, MA, USA) code to produce a smooth BM. Custom FIJI scripts were used to determine the BM opening (BMO) centroid based on BMO markings on the en face view and to generate "virtual" radial scans. These radial scans were centered on the BMO centroid and spaced one degree apart. A Gaussian filter was then applied on the radial OCT stacks for noise reduction.

Visualization and Qualitative Comparisons

For visualization and qualitative comparison between conditions, image volumes were first rotated to align the angle of the peripheral BM in B-scan and orthogonal views. The volumes were rotated to align the blood vessels in the en face view. We then selected corresponding cross sections from OCT scans based on anatomic landmarks, such as arteries and veins. To document the changes throughout the exsanguination process, we selected corresponding B-scans across five timepoints within an eye: alive and after the start of exsanguination (2 seconds, 2 minutes 35 seconds, 3 minutes, and 15 minutes). These five timepoints were considered illustrative of the full set because they corresponded with substantial morphological and physiological changes, such as the collapse of blood vessels.

Delineation and 3D Reconstruction

An experienced observer masked to the experimental condition manually delineated the BM, BMO, inner limiting membrane (ILM), and anterior LC surface (ALC). The structures were delineated in 18 virtual radial sections per scan with the help of custom scripts in FIJI. From these markings, we used custom Matlab routines to reconstruct the structures of interest in 3-D. Eight morphological parameters were analyzed: scleral canal at the BMO (area, planarity, and aspect ratio) and ALC surface (depth, shape index and curvedness, ILM depth, and BM depth). Another five parameters captured the LC visibility, globally, and were split into superior, inferior, nasal, and temporal quadrants. These regions were defined by the BMO centroid and the BMO principal axes such that the major axis corresponded to the superior–inferior orientation. To prevent biases due to sampling density,[22] before measurement, the structures were resampled uniformly.

Repeatability

To determine measurement repeatability, an OCT radial volume (M1 OD, alive) was processed and marked three times for each of the four ONH structures by an observer. Absolute

Investigative Ophthalmology & Visual Science

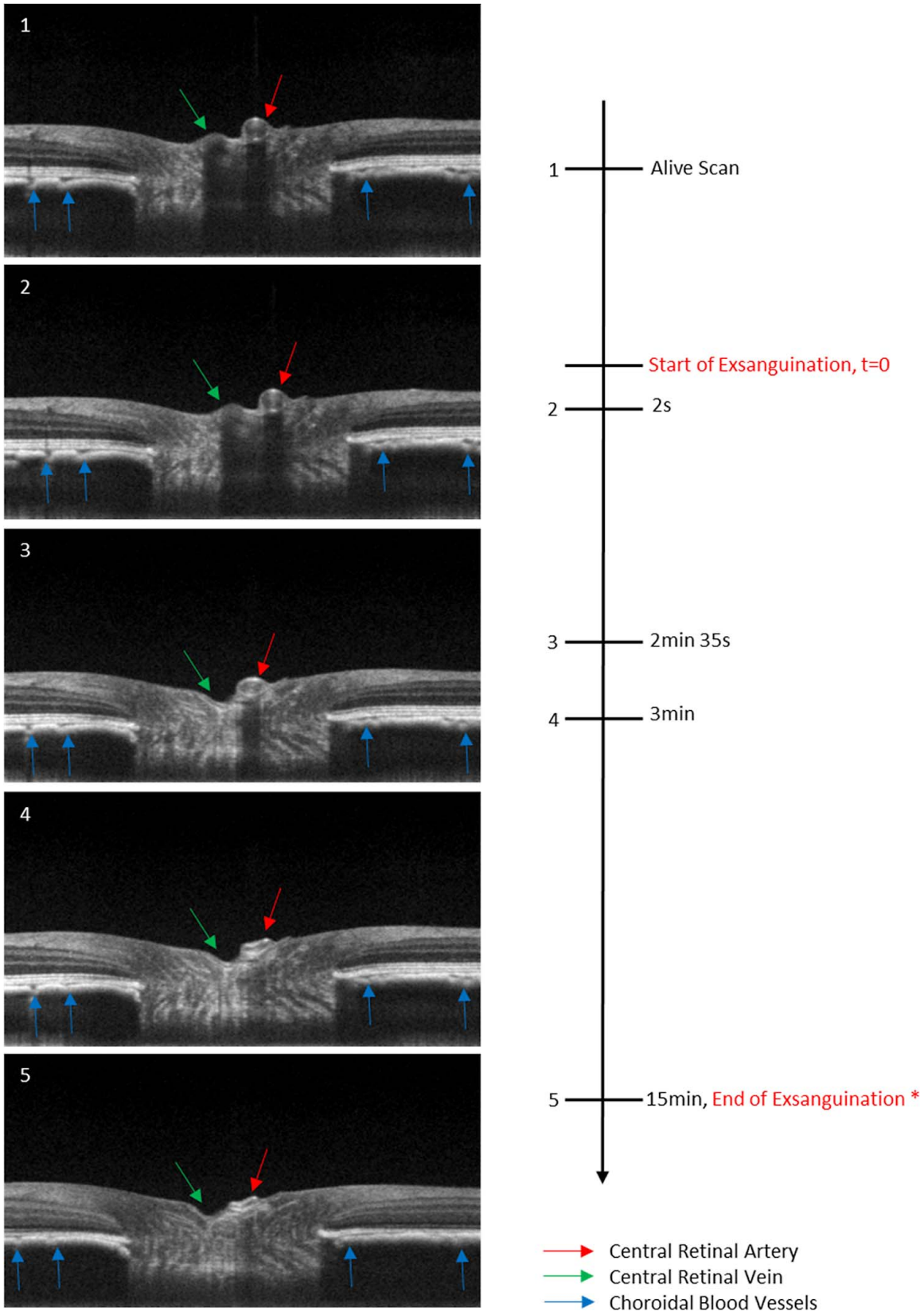

Figure 3. Example B-scans series in an eye. (**1**) Alive, baseline scan taken before the start of exsanguination. (**2**) First scan taken within a few seconds after the start of exsanguination. (**3**) Last scan before collapse of the central artery (*red arrow*); central vein (*green arrow*) has already collapsed, eliminating the shadow underneath and improving ALC visibility. (**4**) First instance of arterial collapse, decreasing the shadow beneath it and further increasing ALC visibility. (**5**) Final scan of the exsanguination series, both the central vein and artery have collapsed, as well as the vessels found within the choroid (*blue arrows*). Throughout the exsanguination series, the brightness of the layers within the sclera can also be seen increasing. *Note that the duration of exsanguination is monkey-dependent.

Investigative Ophthalmology & Visual Science

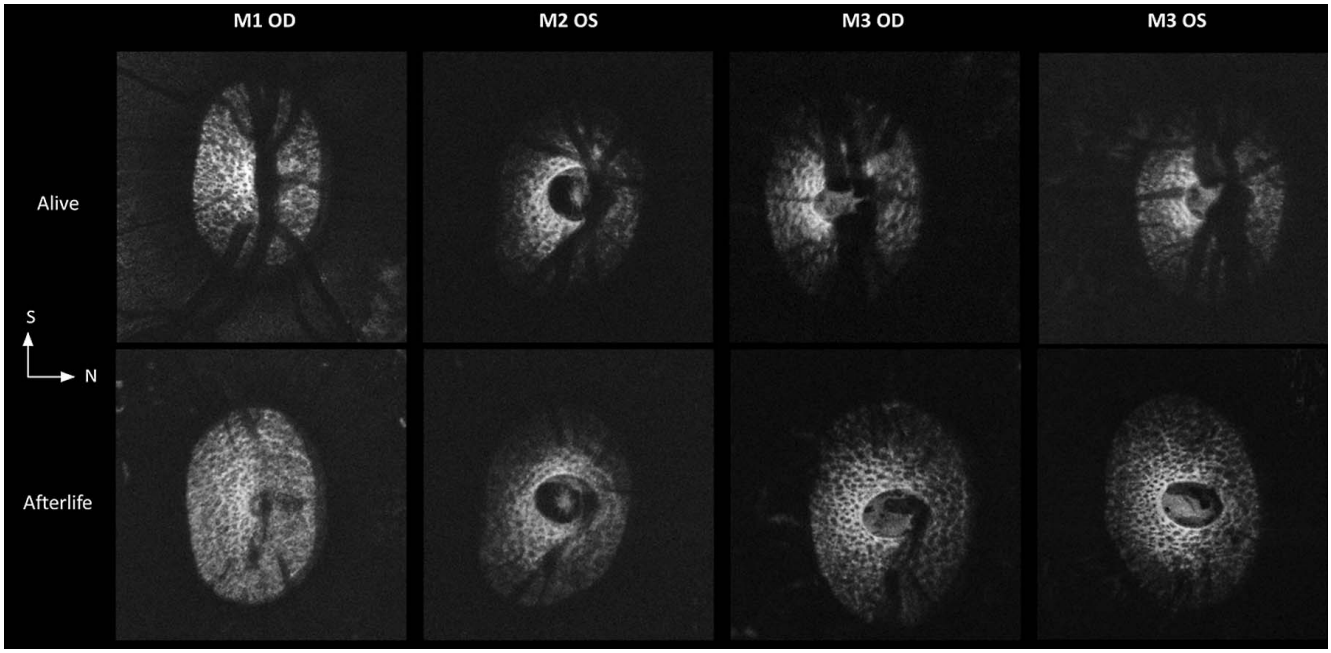

FIGURE 4. Example C-modes at the level of the LC demonstrating substantially improved ALC visibility after life (*bottom row*) relative to the alive condition (*top row*) across all eyes. S, Superior; N, Nasal.

differences and standard deviations among these three marking sets were computed.

Quantitative Analysis: Scleral Canal

A scleral canal reference plane was defined as the best-fit plane to the BMO. The area of the scleral canal was computed as the area of the BMO outline projected onto the reference plane. The planarity of the scleral canal was computed as the average distance from the BMO landmarks to the reference plane. Scleral canal aspect ratio was calculated as the ratio of the major principal axis to the minor principal axis.

Fair comparison between conditions requires comparing only measurements from the same visible region.[23] To do this, the scans of an eye were registered by aligning the BMO center and BMO principal axes and the overlapping regions identified.

Quantitative Analysis: ALC Visibility

The 3-D ALC surface was projected onto the BMO best-fit plane, and the global LC visibility was computed as the ratio between the projected area of the overlapping ALC region for all scans of an eye and the area of the alive scleral canal area in that eye. The overlapping ALC region was the region where the ALC was visible across both alive and after life conditions within an eye. Registered scleral canal planes and ALC surfaces were divided into four quadrants: superior, inferior, nasal, and temporal. These quadrants intersected at the centroid of the scleral canal plane.

Quantitative Analysis: ILM, BM, and ALC Depths

Depths of the ILM, BM, and ALC were calculated with respect to the scleral canal reference plane and only within the overlapping regions of each structure. To distinguish between structures anterior and posterior to the scleral canal plane, we defined depths to be positive as being anterior to the scleral canal.

Quantitative Analysis: LC Shape Index and Curvedness

ALC shape was quantified using shape index and curvedness following previously described methods.[24,25] Briefly, ALC curvatures, k's, were measured every one degree as the inverse radius of a circular arc fit, and the shape index and curvedness of a surface were calculated from the minimum and maximum k's (kmin and kmax, respectively).

$$Shape\ Index(SI) = 2 \times \pi \times \tan^{-1}\left(\frac{kmax + kmin}{kmax - kmin}\right) \quad (1)$$

$$Curvedness(C) = \sqrt{\frac{kmax^2 + kmin^2}{2}} \quad (2)$$

Statistical Analysis

A linear mixed effects model with eye as a random effect was used to determine if LC visibility, by quadrant, was significantly different between alive and after life conditions. The significance threshold was set at 0.05 and then restricted using a Bonferroni adjustment to 0.01, to account for the use of multiple tests. The visibility measurements were transformed to ensure that the errors were homoscedastic (constant variance of the predicted values) and normally distributed. A base 10 logarithm produced a good balance between improving measurement and error distributions and simplicity. To confirm that the results were not tied to the analysis choice, we also calculated a linear model without intercept (a Means model) based on the pooled measurements of LC visibility over the quadrants. For other parameters, because of the small number of eyes studied, the statistical power was insufficient to determine if there were statistically significant differences between the alive and after life conditions. We present the quantitative results and change maps to readers interpret the, sometimes substantial, effects of the exsanguination. Statistical analysis was performed using the R

Investigative Ophthalmology & Visual Science

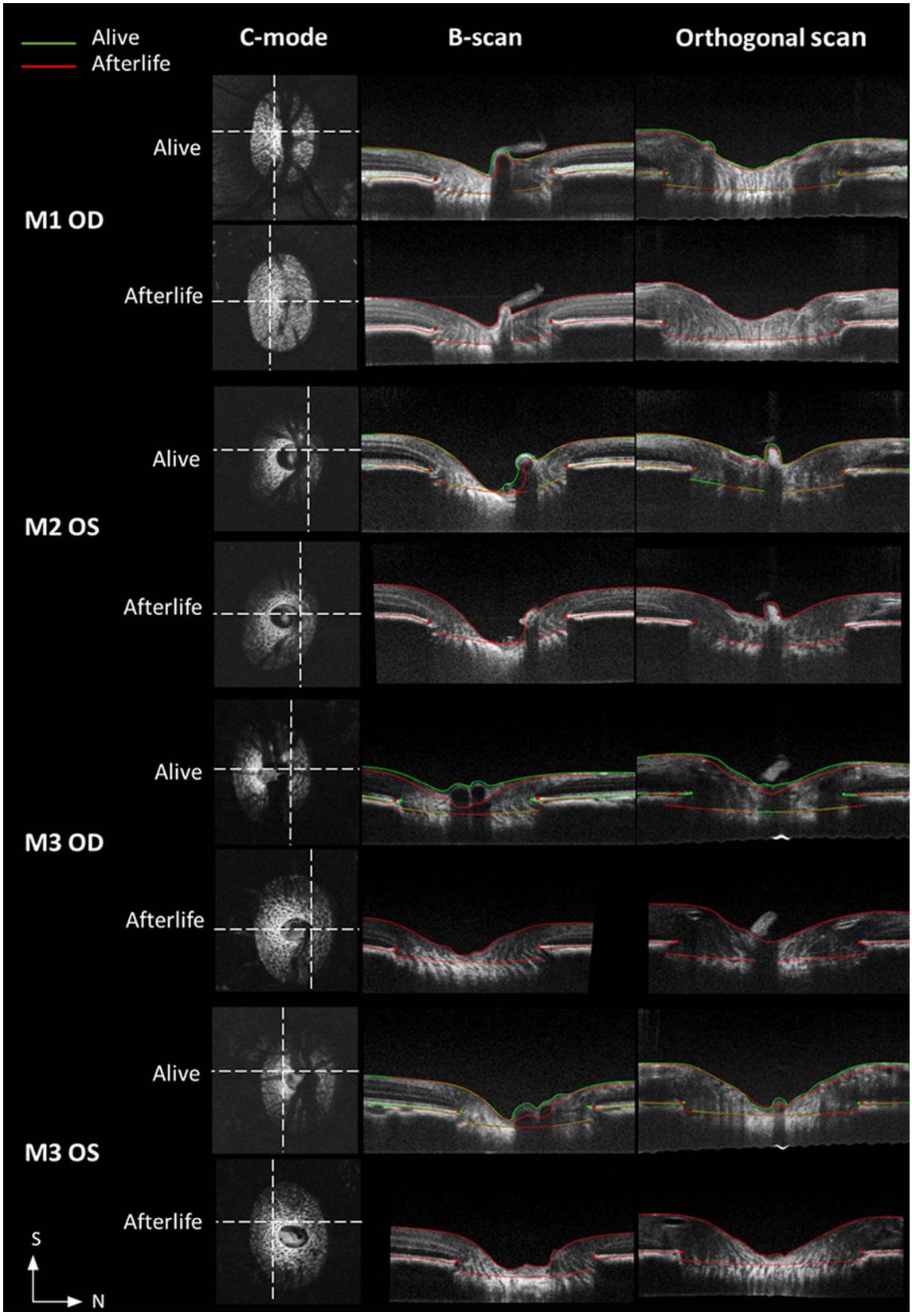

FIGURE 5. Example OCT cross-sections, including C-mode, B-scan, and orthogonal views, for visualizing the ONH and its differences between alive and after life conditions. The longitudinal views are shown with overlaid markings at both alive (*green*) and after life (*red*) conditions. Locations of corresponding longitudinal sections are denoted on C-mode view (*dashed lines*). S, superior; N, nasal.

Investigative Ophthalmology & Visual Science

Table 2. Repeatability Measurements

	BMO			ALC				ILM	BM
Eye, M1 OD	Aspect Ratio	Area, mm^2	Planarity, µm	Median Depth, µm	Global Visibility, %	Shape Index	Curvedness, 10^{-5} $µm^{-1}$	Mean Depth, µm	Mean Depth, µm
Alive: set 1*	1.53	2.09	5.5	−172	93	−0.83	20	331	8.1
Alive: set 2	1.55	2.07	5.6	−162	94	−0.88	22	333	7.1
Alive: set 3	1.53	2.07	4.8	−163	95	−0.88	21	332	6.6
Absolute difference									
Alive: set 2 − set 1	0.02	0.02	0.04	9.9	0.9	0.05	2.1	1.3	1
Alive: set 3 − set 1	−0.004	0.02	0.7	9.3	1.9	0.05	1.4	0.7	1.5
Standard deviation among 3 sets	0.01	0.01	0.44	5.5	1	0.03	1.1	0.7	0.8

* Alive: set 1 is used as data for M1OD Alive condition.

Language and Environment for Statistical Computing program (R Foundation for Statistical Computing, Vienna, Austria).[26]

Results

Visualization and Qualitative Comparisons

In all eyes, there were clear differences in the ONH between alive and after life scans. Specifically, after life there was a substantial decrease in the blood vessel shadows, a collapse of the central retinal and choroidal vessels, and a noticeable improvement in the signal intensities of the retinal layers (Figs. 2–5). In the condition after life, more regions of the LC could be visualized in the OCT images, especially near the central vessels, and in the superior and inferior quadrants, which have substantial shadowing from vasculature when alive. Overlaying markings from both timepoints (before and after death) made the differences easier to discern, evidencing changes in the ONH surface, such as posterior displacement of the central interface between the vitreous and the ONH and an expansion of the scleral canal at the BMO (Fig. 5).

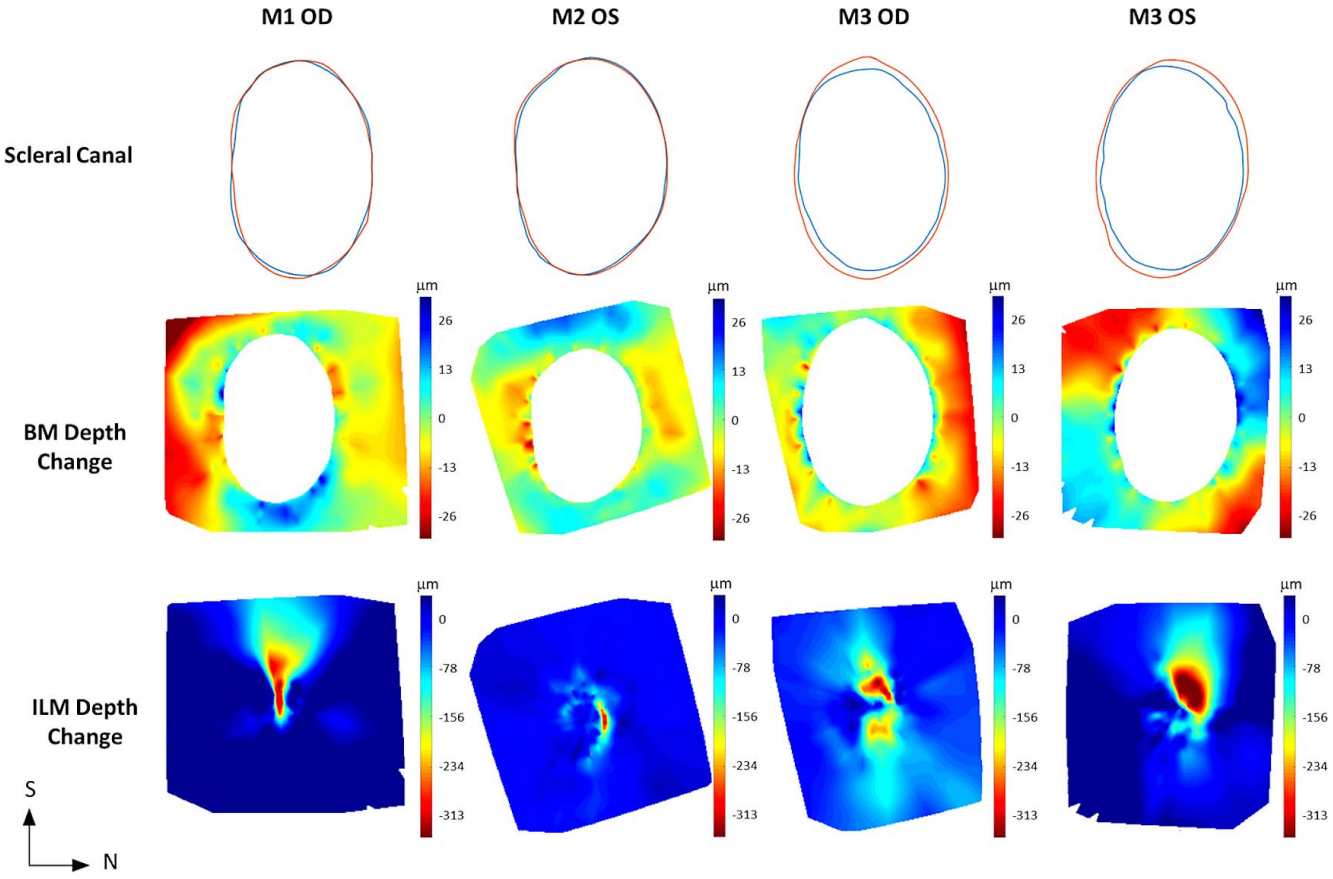

Figure 6. Differences between alive and after life conditions for all eyes in scleral canal area, BM depth, and ILM depth. The top row shows the scleral canal openings, defined at the BMO, when alive (*blue lines*) and after life (*red line*). The middle and bottom rows show the BM and ILM surfaces colored according to the magnitude of the change in depth relative to the BMO reference plane. Positive values indicate changes in the anterior direction. M2 OD and M3 OD presented interesting hourglass patterns. Although the largest changes were concentrated at the location of vessels in the center (note the kidney-shaped changes in M2 OD) and superior sectors of the cup, some still substantial differences more widespread. Corresponding en face images were shown in Figure 4. S, superior; N, nasal.

Table 3. Summary of Measurements

	BMO			ALC				ILM	BM
Eye	Aspect Ratio	Area, mm^2	Planarity, µm	Median Depth, µm	Global Visibility, %	Shape Index	Curvedness, 10^{-5} $µm^{-1}$	Mean Depth, µm	Mean Depth, µm
M1 OD									
Alive	1.53	2.09	5.5	−171	93	−0.83	20	331	8
After life	1.56	2.11	6.9	−166	105	−0.83	24	322	3
Absolute difference	0.02	0.02	1.4	5.6	12	0.004	4.6	9.7	4.7
M2 OS									
Alive	1.42	2.37	7.9	−195	82	−0.87	46	292	21
After life	1.40	2.38	8.5	−201	96	−0.85	40	286	20
Absolute difference	0.02	0.02	0.6	6.5	15	0.015	5.8	5.9	0.5
M3 OD									
Alive	1.38	2.55	4.4	−161	83	−0.81	21	302	4
After life	1.45	2.89	4.5	−159	120	−0.80	20	261	−2
Absolute difference	0.07	0.35	0.1	1.9	37	0.007	1.2	41.5	5.8
M3 OS									
Alive	1.44	2.35	3.5	−156	72	−0.84	21	318	12
After life	1.42	2.66	5.8	−157	118	−0.80	23	283	11
Absolute difference	0.01	0.32	2.3	1.3	45	0.046	2.4	41.5	1.0

Repeatability

Repeatability measures are summarized in Table 2. Note that the voxel edge length of the OCT images was 3.125 µm.

Quantitative Analysis: Scleral Canal

The scleral canals in all four eyes had a larger canal area and higher planarity after death than when alive, with an average increase ranging from 7.2% to 25.2% (Fig. 6, top row; Tables 3, 5). Note that higher planarity values imply that the BMO is more distant from a perfect plane. Canal aspect ratios remained relatively unchanged, with an average increase of 1.1%, reflecting a uniform expansion of the scleral canal.

Table 4. Quadrant ALC Visibility

	Quadrant ALC Visibility, %			
Eye	Superior	Inferior	Nasal	Temporal
M1 OD				
Alive	90	94	111	120
After life	106	113	122	118
M2 OS				
Alive	86	54	72	61
After life	97	81	75	69
M3 OD				
Alive	50	70	80	76
After life	114	116	91	81
M3 OS				
Alive	59	55	53	70
After life	111	112	85	77
	Change in ALC Visibility, %			
M1 OD	17	19	11	−2
M2 OS	12	27	3	8
M3 OD	64	46	10	4
M3 OS	53	56	32	7
Average	36	37	14	4

Quantitative Analysis: ALC Visibility

In all eyes, ALC visibilities were substantially higher in the condition after life, both globally and regionally (Tables 3–5). Globally, ALC visibility increased by an average of 35%. Regionally, there was a substantially larger improvement in visibility in the superior and inferior quadrants compared with the nasal and temporal quadrants, with an average increase of 36%, 37%, 14%, and 4%, respectively. In eye 3 (M3 OD), ALC visibility increased from 50% (alive) to 114% (after life), indicating that the region of the ALC visible after life was even larger than the canal opening recorded when the animal was alive. This represented a direct improvement of 64% and a relative improvement of 228% (the superior ALC area visible after life was 2.28 times larger than that visible when alive). Regions of the ALC with good visibility when alive, especially the temporal side, had only modest changes in visibility.

Statistical Analysis

All four ALC quadrants were shown to have a statistically significant improvement in visibility between alive and after life conditions (Table 6), with a highly significant overall linear mixed effects model (overall $P < 0.0001$). The differences were also significant in the linear intercept Means model (overall $P < 0.001$).

Quantitative Analysis: ILM, BM, and ALC Depths

Changes in ILM, BM, and ALC depths between the alive and after life conditions were very localized (Figs. 6, 7). Specifically, there were orthogonal axes in which one had anterior BM deformation and the other had posterior BM deformations with respect to the scleral canal plane (Fig. 6, middle row). ILM deformations were localized to the central ILM within the scleral canal and the locations of central retinal blood vessels (Fig. 6, bottom row). On average, the median ALC depth had a 0.1% change, whereas the mean ILM and mean BM depths had −7.5% and −55.2% changes, respectively (Tables 3, 5).

Table 5. Percent Changes of ONH Parameters Between Alive and After Life Conditions

	BMO			ALC				ILM	BM
Eye	Aspect Ratio	Area	Planarity	Median Depth	% Visibility	SI	C	Mean Depth	Mean Depth
M1 OD	1.5	0.9	25.1	3.3	12.7	−0.4	23.4	−2.9	−57.8
M2 OS	−1.2	0.7	7.2	−3.4	18.0	1.8	−12.7	−2.0	−2.5
M3 OD	5.0	13.6	2.6	1.2	45.3	0.9	−5.7	−13.7	−152.6
M3 OS	−0.9	13.4	65.9	−0.8	62.8	5.5	11.5	−11.2	−8.0
Average, %	1.1	7.2	25.2	0.1	34.7	1.9	4.1	−7.5	−55.2

SI, shape index.

Quantitative Analysis: LC Shape Index and Curvedness

The shape index of both alive and after life LC ranged from −0.87 to −0.80, indicating cup-like shapes in both conditions (Table 3). Compared to the alive LC, the after life LC had an average increase in shape index and curvedness of 1.9% and 4.1%, respectively (Table 5).

Discussion

Summary

Our study achieved two important goals. First, we demonstrated an experimental approach that allows direct comparison of primate ONHs before and after death. Second, we demonstrated that exsanguination improved LC visibility with OCT. Qualitative comparison of the OCT scans reveals that the ONH structures after death look similar, but not identical, to the structures while alive. In the after life scans, the blood vessel shadowing was clearly diminished, with evident collapse of the central retinal vessels and choroid, as well as some discernible changes in the signal intensity of the retinal layers. Quantitatively, death by exsanguination resulted in a substantial and significant improvement on ALC visibility. On average, ALC visibility increases by 35% in the after life scans compared with those in the alive condition. The largest increases were in the superior and inferior quadrants, in which the visible ALC area increased by 36% and 37%, respectively. In M3 OD, the visibility in the superior quadrant increased by 228%. ALC visibility in the nasal and temporal quadrants also increased, but the changes were far less marked, 14% and 4%, respectively, in large part because visibility in these quadrants was already good when alive.

Table 6. Linear Mixed Effects Model of Quadrant LC Visibility

		Confidence Interval		
Effect	Estimate	2.5%	97.5%	*P*
Fixed effects				
Quadrant LC visibility				
Inferior	3.52	2.67	4.37	<0.0001
Nasal	2.32	1.47	3.17	0.0002
Superior	3.36	2.51	4.21	<0.0001
Temporal	1.53	0.68	2.38	0.0029
Random effect				
Eye	0.47	0.15	1.45	

Fixed effects were log-transformed of LC visibility in each of the four quadrants: superior, inferior, nasal, and temporal. Results shown were the estimated means for each quadrant with 95% confidence intervals for each mean. Significant level after Bonferroni correction to adjust for multiple measures per eye was $P = 0.001$.

We also quantitatively analyzed eight parameters describing ONH morphology. For some of these parameters, the differences were consistent and substantial. After life scleral canals were larger, with 7.2% increase in area, and less flat, with 25.2% increase in planarity, but similar in shape, with only 1.1% increase in aspect ratio. After life ALCs were slightly curvier, with 4.1% increase in curvedness, and less cup-like, with 1.9% increase in shape index, but had minimal (0.1%) change in depth with respect to the scleral canal. Compared to those in the alive condition, in the after life scans, the BM and the interface between vitreous and optic nerve head deformed to be closer to the scleral canal, with average decreases of 55.2% and 7.5%, respectively.

Because of the small number of eyes studied herein, the statistical power was not sufficient to determine statistical significance in the presence of wide variability in ONH morphology. Some of the morphologic differences were small and within, or close to, the margin of repeatability, and, therefore, the differences observed should be interpreted carefully. For example, absolute differences in ALC depth between alive and after life conditions ranged between 1.3 μm and 6.5 μm over the eyes, whereas the standard deviation of the repeatability measurements was 5.5 μm. Nevertheless, our results serve as proof that, at least in some eyes, with death by exsanguination, there are marked changes in ONH morphology, specifically, in canal area and planarity and BM depth.

Discussion of Relevance and Strengths

Our study provides the first detailed measurements of after life in-situ ONH structures as well as the first comparison of alive versus after life conditions in same eye. A key feature of our approach is that it enhances visibility of LC regions that are not typically visible in OCT. This enhanced LC visibility is relevant in many aspects of basic and clinically relevant research in which the LC is of interest.[15,27,28] For example, it will allow better characterization of the LC, especially in ONH regions of early glaucomatous damage.[4] Another strength of our study is that ONH morphology was measured in 3-D by using OCT volumes. The ONH is intrinsically a 3-D structure, and capturing its morphology in 3-D renders more robust measurements and a better representation to the actual morphology than 2-D approximations.[10,22,29–31]

While the specific differences in ONH morphology between alive and after life conditions that we documented have important applications in future research in ocular biomechanics, the existence of differences should not come as a surprise, as there are sound reasons that suggest that this would be the case. The exsanguination process removes the effects of blood pressure, which could directly lead to deformations. Also, the absence of blood pressure could affect the mechanical support from the central retinal vessels to the LC.[32–34] Previous studies had also shown that the central retinal vessels' diameter and location within the LC is associated with the location and amount of glaucomatous damage.[35,36] We performed the

Investigative Ophthalmology & Visual Science

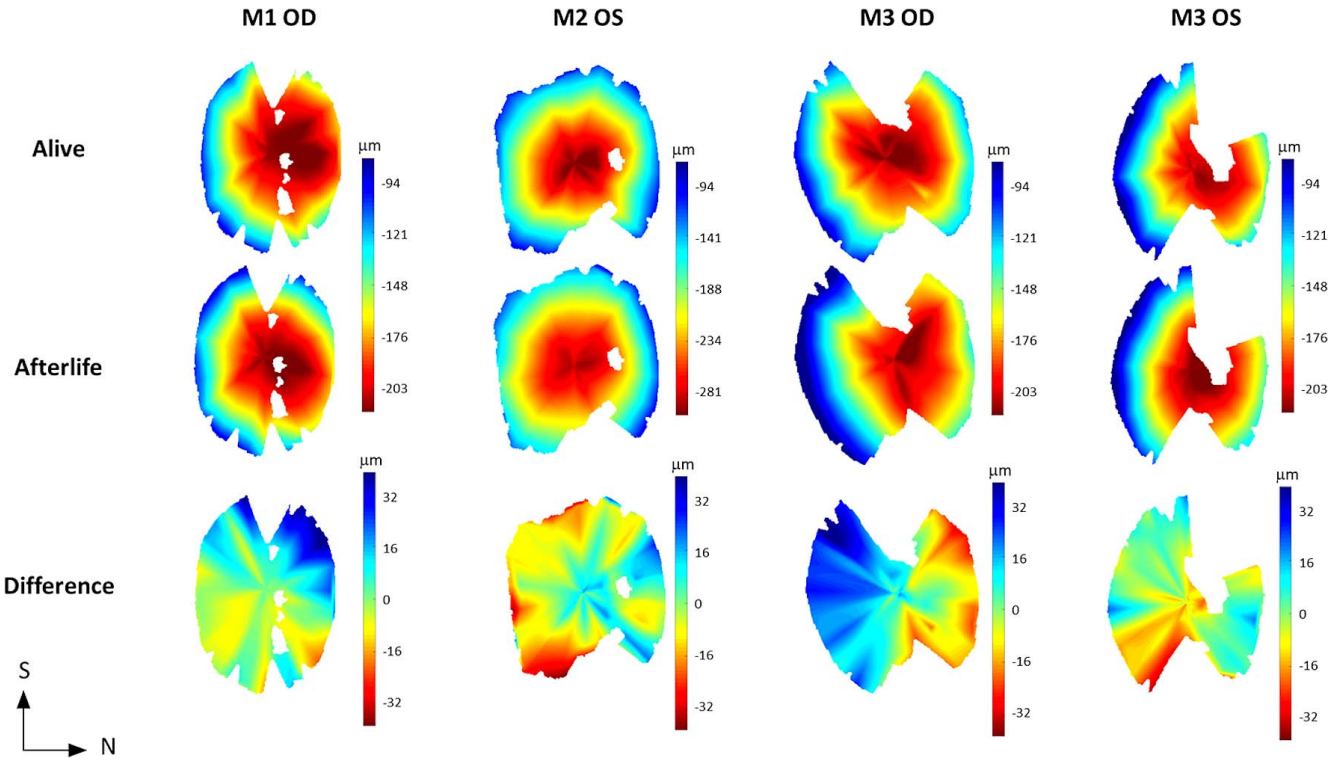

Figure 7. ALC depth in the alive (*top row*) and after life (*middle row*) conditions and the difference (*bottom row*). Note that, here, we only show the ALC surface that was visible in all scans. Note that, in addition to the alive/after life states, there were differences in IOP and ICP between the conditions (Table 3). Corresponding en face images were shown in Figure 4. S, superior; N, nasal.

exsanguination with two different locations of the arterial line and noticed that the animals with the arterial line placed in the carotid artery had a shorter exsanguination timeline than the one placed in the femoral artery. We suspect that the carotid setting might have induced a more abrupt ischemia, whereas the femoral setting was more gradual and thus resulted in a longer exsanguination timeline. Coupled with viscoelastic properties of the tissues of the ONH, this could change the alive versus after life changes measured. In addition, despite measurements in situ and with the use of a paralytic, there may also be differences in muscle tone between alive and after life conditions. Note that the eyes had different IOP and ICP at the time of imaging, and it seems plausible that this would also have an effect on the ONH shape.[32–34,37,38] The combined effects of IOP and ICP on the monkey ONH remain unclear and should be further investigated.

Limitations

It is important to consider the limitations of our study when interpreting the results. First, it is the small sample size of four eyes from three monkeys. Nevertheless, we believe that this should be weighed with the improved relevance in the use of a species that shares key similarities in anatomy and physiology with humans. Second, there was no IOP cannulation in the last monkey (M3), which could have contributed to the variability in how the ONH structures responded to exsanguination. Elsewhere, we have shown that variations in one pressure may have both direct effects on ONH morphology and also indirect effects by modifying the effects of other pressures.[34,39,40] Exsanguination results in a drop in vascular tone, which directly affects vessels, as mentioned above, and may also impact the ONH indirectly by affecting how IOP and/or ICP affect the ONH, and even further by affecting IOP and/or ICP and cerebrospinal fluid pressures. The important task of elucidating the full effects of IOP, ICP, and blood pressure, independently or in interaction, requires a careful and systematic approach beyond the scope of this study. There may be other methods that are less likely to cause changes to the ONH and LC. Note that other methods to cause death will still likely result in similar loss of vascular pressure and blood drainage. Here, we chose a specific approach of exsanguination with several advantages, including that the eyes were imaged in situ instead of ex vivo, there were active controls of both IOP and ICP, and there was close monitoring of heart rate and blood pressure.

Ex vivo studies using enucleated eyes will suffer from much more substantial changes in environment and other conditions and should be expected to differ even more from the in vivo conditions. Hence, the in situ changes that we document represent a lower boundary for differences between in vivo and ex vivo.

Naturally, we do not to propose exsanguination as a method to improve LC visibility in subjects imaged with OCT. Our technique, however, could be applicable in animal models, many of which include terminal experiments. Additionally, histologic studies of tissues sometimes, but not always, are based on eyes that were perfusion fixed. Future studies could explore if those suffer similar changes in morphology as observed here. Furthermore, much of what is known about the ONH is from ex vivo studies, and, therefore, it is critical to determine the differences in vivo versus ex vivo. We have demonstrated that it is possible to detect differences between the alive and after life scans obtained in situ of the same eye.

Investigative Ophthalmology & Visual Science

Summary

We have demonstrated an experimental approach for spectral-domain OCT imaging before and after death by exsanguination. Using this method, we report significant increases in ALC visibility in all four quadrants, as well as detectable and sometimes consistent ONH morphologic changes between alive and after life conditions. Our approach will allow for improved characterization of the LC, especially of the superior and inferior LC regions that are usually blocked by blood vessel shadows when imaging with OCT. Our measurements also point to changes in ONH morphology with the loss of blood pressure. Future research will be needed to determine whether there are differences in ONH biomechanics between alive and after life conditions and what those differences would imply.

Acknowledgments

Supported by National Institutes of Health (R01EY025011, R01EY03966, T32-EY017271, R01-EY013178, P30-EY008098, and R01EY022928), Glaucoma Research Foundation Shaffer Grant, and Eye and Ear Foundation of Pittsburgh (PA, USA).

Disclosure: **H. Tran**, None; **J. Wallace**, None; **Z. Zhu**, None; **K.A. Lucy**, None; **A.P. Voorhees**, None; **S.E. Schmitt**, None; **R.A. Bilonick**, None; **J.S. Schuman**, P; **M.A. Smith**, None; **G. Wollstein**, None; **I.A. Sigal**, None

References

1. Wang B, Nevins JE, Nadler Z, et al. In vivo lamina cribrosa micro-architecture in healthy and glaucomatous eyes as assessed by optical coherence tomography. *Invest Ophthalmol Vis Sci*. 2013;54:8270–8274.
2. Yang H, Williams G, Downs JC, et al. Posterior (outward) migration of the lamina cribrosa and early cupping in monkey experimental glaucoma. *Invest Ophthalmol Vis Sci*. 2011;52:7109–7121.
3. Albon J, Purslow PP, Karwatowski WS, Easty DL. Age related compliance of the lamina cribrosa in human eyes. *Br J Ophthalmol*. 2000;84:318–323.
4. Quigley HA, Addicks EM. Regional differences in the structure of the lamina cribrosa and their relation to glaucomatous optic nerve damage. *Arch Ophthalmol*. 1981;99:137–143.
5. Jones HJ, Girard MJ, White N, et al. Quantitative analysis of three-dimensional fibrillar collagen microstructure within the normal, aged and glaucomatous human optic nerve head. *J R Soc Interface*. 2015;12:20150066.
6. Strouthidis NG, Fortune B, Yang H, Sigal IA, Burgoyne CF. Longitudinal change detected by spectral domain optical coherence tomography in the optic nerve head and peripapillary retina in experimental glaucoma. *Invest Ophthalmol Vis Sci*. 2011;52:1206–1219.
7. Whitford C, Joda A, Jones S, Bao F, Rama P, Elsheikh A. Ex vivo testing of intact eye globes under inflation conditions to determine regional variation of mechanical stiffness. *Eye Vis*. 2016;3:21.
8. Coudrillier B, Campbell IC, Read AT, et al. Effects of peripapillary scleral stiffening on the deformation of the lamina cribrosa. *Invest Ophthalmol Vis Sci*. 2016;57:2666–2677.
9. Voorhees AP, Ho LC, Jan NJ, et al. Whole-globe biomechanics using high-field MRI. *Exp Eye Res*. 2017;160:85–95.
10. Yang H, Downs JC, Sigal IA, Roberts MD, Thompson H, Burgoyne CF. Deformation of the normal monkey optic nerve head connective tissue after acute IOP elevation within 3-D histomorphometric reconstructions. *Invest Ophthalmol Vis Sci*. 2009;50:5785–5799.
11. Kimball EC, Nguyen C, Steinhart MR, et al. Experimental scleral cross-linking increases glaucoma damage in a mouse model. *Exp Eye Res*. 2014;128:129–140.
12. Ostrin LA, Wildsoet CF. Optic nerve head and intraocular pressure in the guinea pig eye. *Exp Eye Res*. 2016;146:7–16.
13. Hiraoka M, Inoue K, Ninomiya T, Takada M. Ischaemia in the Zinn-Haller circle and glaucomatous optic neuropathy in macaque monkeys. *Br J Ophthalmol*. 2012;96:597–603.
14. Hussain AA, Lee Y, Zhang J-J, Marshall J. Characterization of the gelatinase system of the laminar human optic nerve, and surrounding annulus of Bruch's membrane, choroid, and sclera. *Invest Ophthalmol Vis Sci*. 2014;55:2358–2364.
15. Sigal IA, Wang B, Strouthidis NG, Akagi T, Girard MJA. Recent advances in OCT imaging of the lamina cribrosa. *Br J Ophthalmol*. 2014;98(suppl 2):ii34–ii39.
16. Girard MJA, Strouthidis NG, Desjardins A, Mari JM, Ethier CR. In vivo optic nerve head biomechanics: performance testing of a three-dimensional tracking algorithm. *J R Soc Interface*. 2013;10:20130459.
17. Voorhees AP, Jan N-J, Austin ME, et al. Lamina cribrosa pore shape and size as predictors of neural tissue mechanical insult. *Invest Ophthalmol Vis Sci*. 2017;58:5336–5346.
18. Grytz R, Meschke G, Jonas JB. The collagen fibril architecture in the lamina cribrosa and peripapillary sclera predicted by a computational remodeling approach. *Biomech Model Mechanobiol*. 2011;10:371–382.
19. Girard MJA, Strouthidis NG, Ethier CR, et al. Shadow removal and contrast enhancement in optical coherence tomography images of the human optic nerve head. *Invest Ophthalmol Vis Sci*. 2011;52:7738–7748.
20. Zhang M, Hwang TS, Campbell JP, et al. Projection-resolved optical coherence tomographic angiography. *Biomed Opt Express*. 2016;7:816.
21. Sigal IA, Grimm JL, Schuman JS, Kagemann L, Ishikawa H, Wollstein G. A method to estimate biomechanics and mechanical properties of optic nerve head tissues from parameters measurable using optical coherence tomography. *IEEE Trans Med Imaging*. 2014;33:1381–1389.
22. Sigal IA, Flanagan JG, Tertinegg I, Ethier CR. 3D morphometry of the human optic nerve head. *Exp Eye Res*. 2010;90:70–80.
23. Nadler Z, Wang B, Schuman JS, et al. In vivo three-dimensional characterization of the healthy human lamina cribrosa with adaptive optics spectral-domain optical coherence tomography. *Invest Ophthalmol Vis Sci*. 2014;55:6459–6466.
24. Koenderink JJ, van Doorn AJ. Surface shape and curvature scales. *Image Vis Comput*. 1992;10:557–564.
25. Thakku SG, Tham YC, Baskaran M, et al. A global shape index to characterize anterior lamina cribrosa morphology and its determinants in healthy Indian eyes. *Invest Ophthalmol Vis Sci*. 2015;56:3604–3614.
26. R Core Team. R: a language and environment for statistical computing. R Foundation for Statistical Computing: Vienna, Austria; 2013.
27. Dong ZM, Wollstein G, Wang B, Schuman JS. Adaptive optics optical coherence tomography in glaucoma. *Prog Retin Eye Res*. 2017;57:76–88.
28. Park SC. In vivo evaluation of lamina cribrosa deformation in glaucoma. *J Glaucoma*. 2013;22Suppl 5:S29–31.
29. Sredar N, Ivers KM, Queener HM, Zouridakis G, Porter J. 3D modeling to characterize lamina cribrosa surface and pore geometries using in vivo images from normal and glaucomatous eyes. *Biomed Opt Express*. 2013;4:1153–1165.
30. Girkin CA, Fazio MA, Yang H, et al. Variation in the three-dimensional histomorphometry of the normal human optic nerve head with age and race: lamina cribrosa and peripapillary scleral tThickness and position. *Invest Ophthalmol Vis Sci*. 2017;58:3759–3769.

31. Sigal IA, Flanagan JG, Lathrop KL, Tertinegg I, Bilonick R. Human lamina cribrosa insertion and age. *Invest Ophthalmol Vis Sci*. 2012;53:6870–6879.
32. Sigal IA, Ethier CR. Biomechanics of the optic nerve head. *Exp Eye Res*. 2009;88:799–807.
33. Burgoyne CF, Downs JC, Bellezza AJ, Suh J-KF, Hart RT. The optic nerve head as a biomechanical structure: a new paradigm for understanding the role of IOP-related stress and strain in the pathophysiology of glaucomatous optic nerve head damage. *Prog Retin Eye Res*. 2005;24:39–73.
34. Hua Y, Voorhees AP, Grimm JL, Yang B, Schuman JS, Sigal IA. Cerebrospinal fluid pressure (CSFP) and the constraints on the optic nerve at the orbit exit (CON) can influence optic nerve head (ONH) biomechanics. *Invest Ophthalmol Vis Sci*. 2017;58:3172.
35. Jonas JB, Budde WM, Németh J, Gründler AE, Mistlberger A, Hayler JK. Central retinal vessel trunk exit and location of glaucomatous parapapillary atrophy in glaucoma. *Ophthalmology*. 2001;108:1059–1064.
36. Jonas JB, Fernández MC. Shape of the neuroretinal rim and position of the central retinal vessels in glaucoma. *Br J Ophthalmol*. 1994;78:99–102.
37. Wang B, Tran H, Smith MA, et al. In-vivo effects of intraocular and intracranial pressures on the lamina cribrosa microstructure. *PLoS One*. 2017;12:1–16.
38. Tran H, Grimm J, Wang B, et al. Mapping in-vivo optic nerve head strains caused by intraocular and intracranial pressures. *Proc SPIE Int Soc Opt Eng*. 2017;10067:100670B.
39. Sigal IA. Interactions between geometry and mechanical properties on the optic nerve head. *Invest Ophthalmol Vis Sci*. 2009;50:2785–2795.
40. Sigal IA, Yang H, Roberts MD, Burgoyne CF, Downs JC. IOP-induced lamina cribrosa displacement and scleral canal expansion: an analysis of factor interactions using parameterized eye-specific models. *Investig Opthalmology Vis Sci*. 2011;52:1896.

Investigative Ophthalmology & Visual Science